

Supplementary Information

Organic photo-battery with high operating voltage using a multi-junction organic solar cell and an organic redox-polymer-based battery

Rodrigo Delgado Andrés[†], Robin Wessling[†], Jan Buettner, Leonie Pap, Anna Fischer, Birgit Esser*, Uli Würfel*

[†]These authors contributed equally to this work

*Corresponding authors

Table of Contents

1. Multi-junction solar cell characterization.....	S1
2. Calculation of V_{OC} in multi-junction cells	S5
3. Simulation details for multi-junction cells.....	S6
4. Prototype cell housing	S8
5. Characterization of the separate parts of the photo-battery	S10
6. Additional photo-battery data.....	S12
7. Total cycle efficiency calculation.	S13
8. Ragone plot for photocharge cycling the photo-battery.....	S14
9. Redox equations for the charging and discharging processes	S15
10. Comparison of multi-junction solar cells from the literature.....	S16
11. Comparison of photo-chargeable devices from the literature.....	S17
12. References	S18

1. Multi-junction solar cell characterization

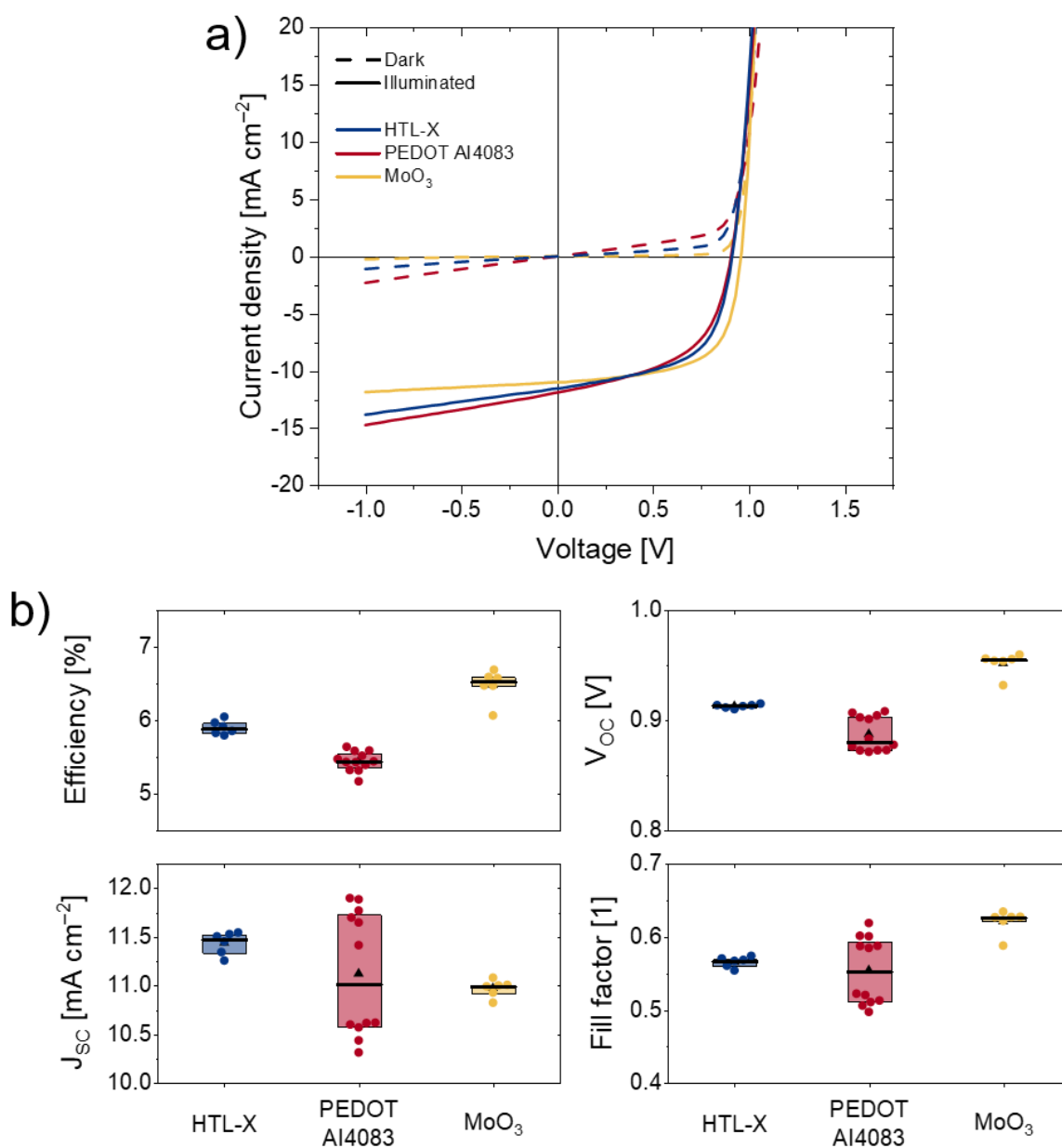


Figure S1: Characterization results of single junction OSC with different HTLs. a) JV-curve of single-junction inverted OSCs with different HTLs. Notice that for these first test on single-junction cells, the parallel resistance (R_p) of the devices using PEDOTs formulation as HTL was very low, and that by correcting for this fact, the results for all HTLs are very similar. The reasons behind this are likely the poor coverage and the existence of pinholes, although for this particular blend the values of R_p appear to be particularly low, regardless of the HTL used. b) Summary of the parameters extracted from the JV-curves.

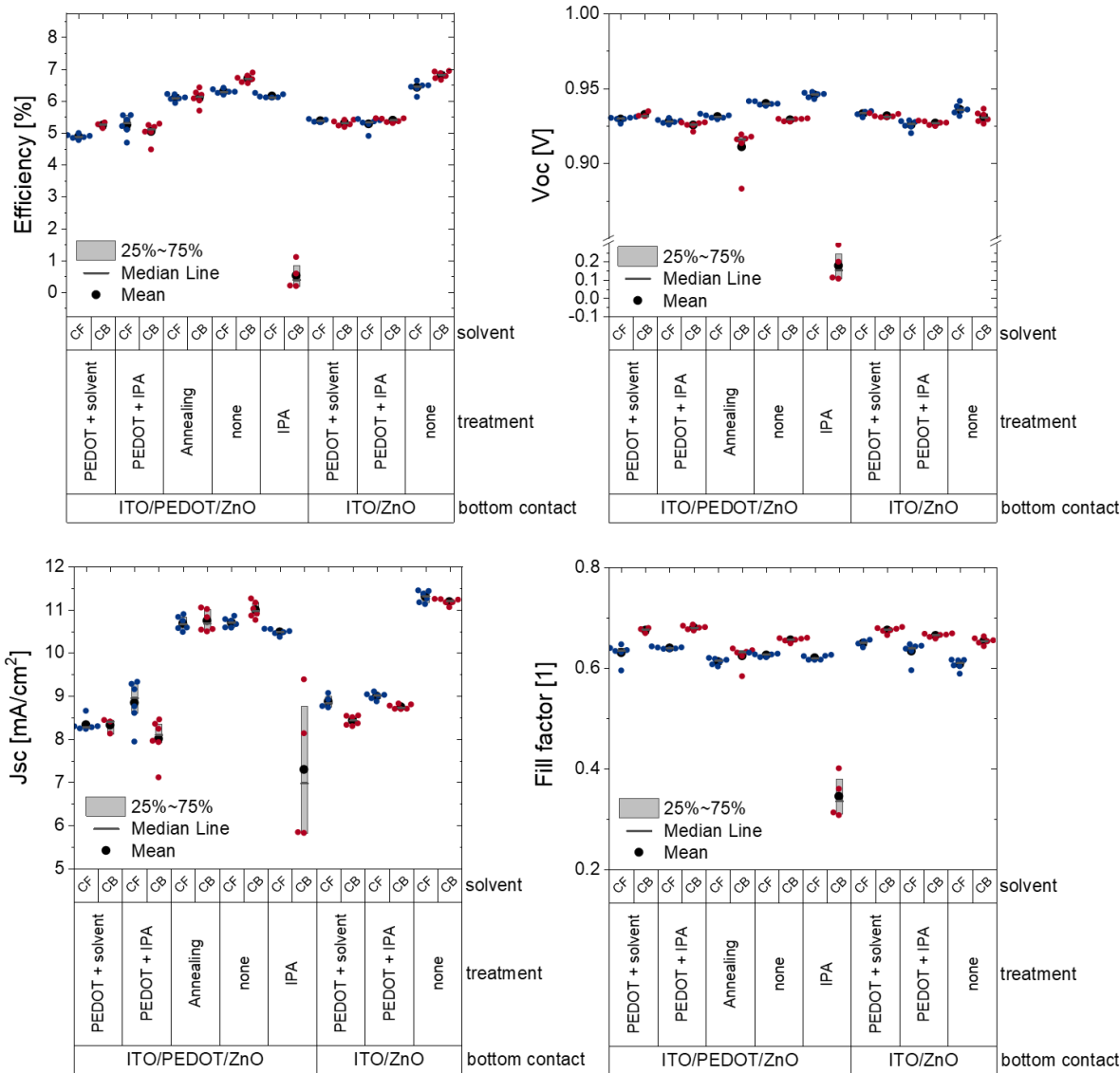


Figure S2: Resulting parameters from solar cells subjected to different treatments to simulate processing damage. Because damage can be induced to either the blend layer or the ICL, two types of bottom contacts were used: ITO/ZnO, same used for single junction cell and ITO/PEDOT/ZnO, to reproduce the effect of having a ICL. Two solvents were used for casting the active layers, chlorobenzene (CB) and chloroform (CF). In all cases the “treatment” corresponds to different actions taken after the blend layer deposition. “PEDOT+solvent” involves spin coating a PEDOT layer and on top of it the blend solvent. “PEDOT+IPA” similarly spin coating PEDOT and immediately after isopropanol. The “Annealing” treatment corresponds to annealing after active layer deposition for 1 h at 120 °C. This corresponds to the total annealing time that the first junction in a 5-junction stack is subjected to during fabrication. “IPA” treatment involves spin coating isopropanol on the freshly coated active layer. Only one of the treatments (“IPA”) caused a severe voltage loss. Because this solvent is used in both the PEDOT AI mixture and the ZnO NP dispersion, this could be an indication that processing of these layers can cause pinholes. Nevertheless, when the PEDOT layer was introduced (“PEDOT+IPA”) there was no indication of this voltage loss, suggesting that the PEDOT can provide some protection.

Table S1: Detailed performance values for the HTL optimization shown in Figure 2.

HTL	J_{sc} [mA/cm ²]	V_{oc} [V]	FF	Eff. [%]
HTL-X	9.1	0.86	0.42	3.3
Al4083	6.9	1.53	0.46	4.9
MoO3	6.6	1.61	0.55	5.9

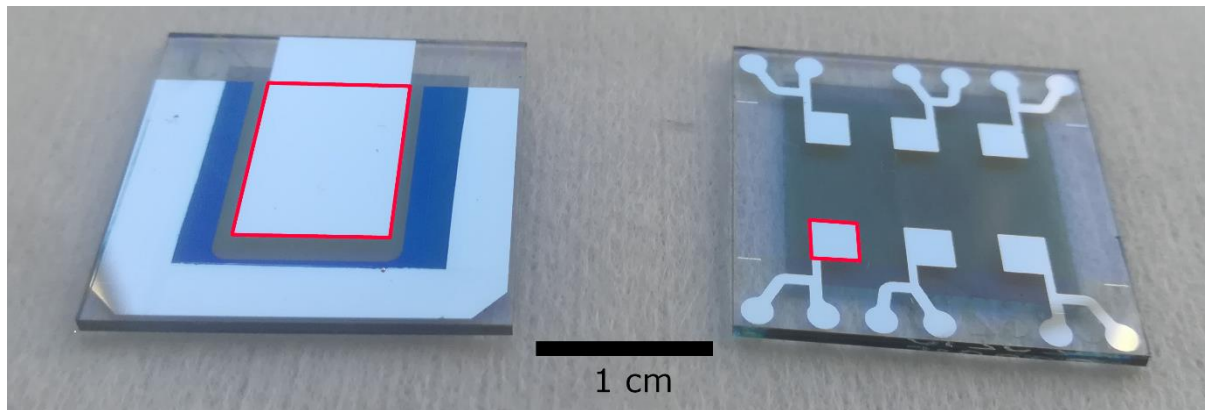


Figure S3: Solar cell geometry as used during experiments in single-junction as well as multi-junction cells (picture shows single-junction, but multi-junction geometry is identical). The red rectangles show the active area as defined by the top metal contact. Left, the upscaled cell with area 1.2 cm², used for the assembly of the PB. Right, the cell (with 6 cells on a substrate) used for optimization of the multi-junction parameters.

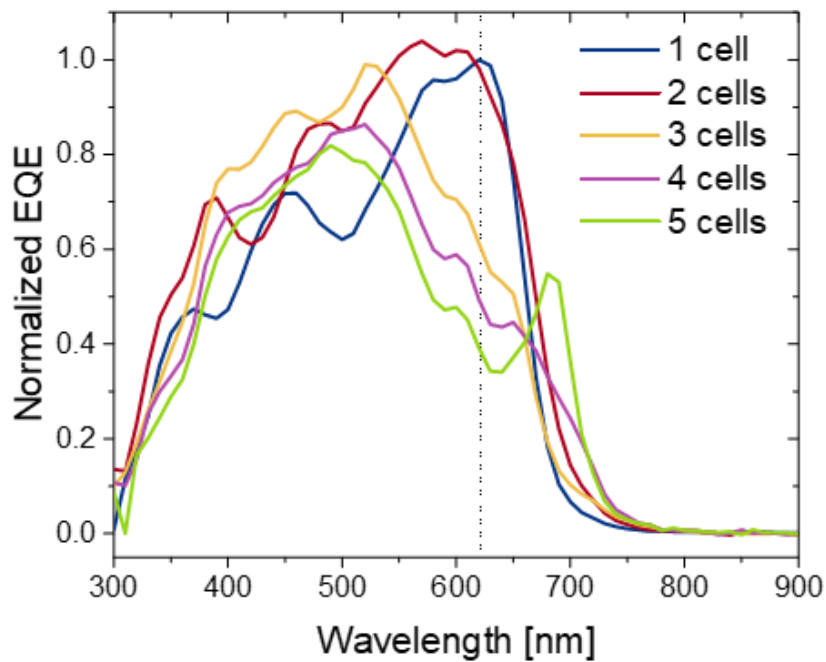


Figure S4: Normalized EQE spectra for devices with increasing number of junctions. The different spectra are normalized to the “1-cell” spectra, and multiplied by the number of sub-cells.

Table S2: Detailed performance values for the variation of the number of sub cells shown in figure 3.

# Junctions	J_{sc} [mA/cm ²]	V_{oc} [V]	FF	Eff. [%]
1	11.7	0.918	0.66	7.2
2	6.8	1.77	0.63	7.6
3	3.9	2.27	0.62	5.6
4	2.1	2.78	0.65	3.9
5	1.2	3.20	0.64	2.6

2. Calculation of V_{OC} in multi-junction cells

For a single junction cell, both J_{SC} and V_{OC} are known from measurements. Starting with the ideal one-diode equation (Equation S1), it can be solved for the dark saturation current J_0 , by setting $J = 0$ and $V = V_{OC}$ (open-circuit conditions).

$$J(V) = J_{SC} + J_0 \left[\exp\left(\frac{qV}{kT}\right) - 1 \right] \quad \text{Equation S1}$$

For a larger number of sub cells, only the total J_{SC} and V_{OC} of the stack can be measured. The individual contribution of each cell can only be estimated by taking several assumptions. We proceeded as follows: first, the dark saturation current for each sub cell is the same as for the single junction cell. Second, the sub cell limiting the current is always the top cell in the stack, i.e., the farthest cell from the illuminated electrode. This last assumption is confirmed to be correct by optical simulations.

In this scenario, for multi-junction cells, the V_{OC} of the top sub cell can then always be estimated from the J_{SC} of the complete stack, reorganizing Equation S1 to solve for the voltage as:

$$V_{OC} = \frac{kT}{q} \ln\left(1 + \frac{J_{SC}}{J_0}\right) \quad \text{Equation S2}$$

Thus, manufacturing multi-junctions with increasing number of junctions (2, 3, 4 and 5) we can estimate the progression of the voltage from the photogenerated current.

3. Simulation details for multi-junction cells

For performing the optical simulations, we used the refractive indices n and the extinction coefficients k of all layers, extracted from UV/Vis spectroscopy and thickness measurements, as well as the simulation software SCOUT, which calculates the resulting currents for a given layer thickness under the assumption of an internal quantum efficiency of unity using the transfer matrix method. The results of such simulations are summarized in the following.

Since the optical simulations only return the expected current for a given active layer thickness, the expected voltage used for comparison was calculated based on the fact that under open-circuit conditions, there is an equilibrium between generation and recombination of charges. The recombination properties of the device are thereby extracted from the single-junction solar cell using the one-diode equation, as detailed above.

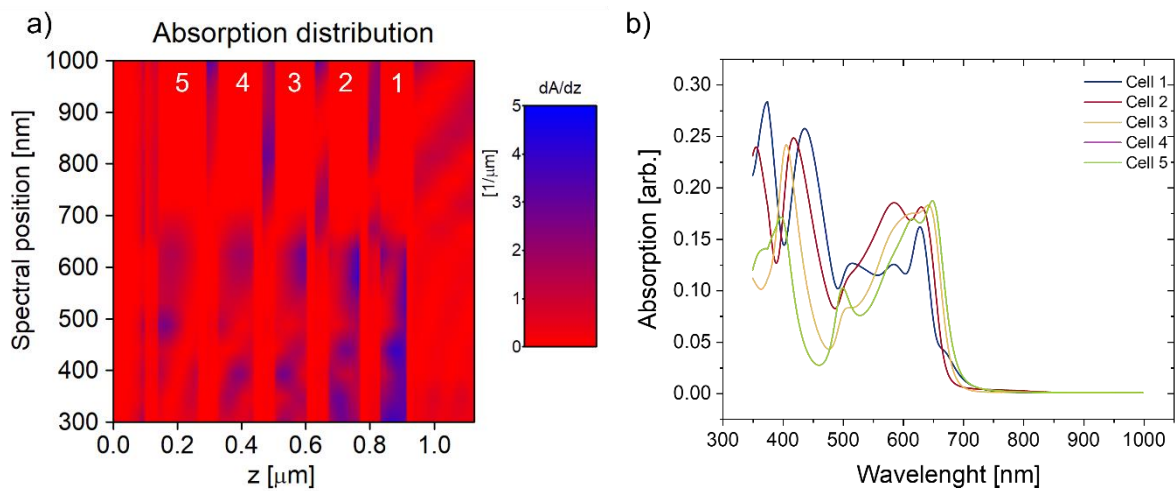


Figure S5: a) Simulated absorption distribution for a 5-junction stack. Light enters the device from the right, and the cells are numbered accordingly from 1 to 5. b) Simulated absorption spectra for each cell in the 5-junction stack.

Table S3: Simulation results for a 3 sub-cells stack using PM6:PC₆₀BM. The cell number corresponds to the position in the stack with respect to the illuminated side. For the experimental values, only the resulting current density for the whole stack is known.

Simulation			
Cell number	1	2	3
Thickness [nm]	80	100	110
Current Density [mA/cm ²]	4.36	4.16	3.96
Experimental			
Cell number	1	2	3
Thickness [nm]	75	92	92
Current Density [mA/cm ²]	3.96		

Table S4: Simulation results for a 4 sub cells stack using PM6:PC₆₀BM. The cell number corresponds to the position in the stack with respect to the illuminated side. For the experimental values, only the resulting current density for the whole stack is known.

Simulation				
Cell number	1	2	3	4
Thickness [nm]	80	100	100	110
Current Density [mA/cm²]	2.9	3.54	3.05	2.8
Experimental				
Cell number	1	2	3	4
Thickness [nm]	75	92	92	98
Current Density [mA/cm²]	2.15			

Table S5: Simulation results for a 5 sub cells stack using PM6:PC₆₀BM. The cell number corresponds to the position in the stack with respect to the illuminated side. For the experimental values, only the resulting current density for the whole stack is known.

Simulation					
Cell number	1	2	3	4	5
Thickness [nm]	80	100	100	110	125
Current Density [mA/cm²]	2.82	2.66	2.37	2.25	2.18
Experimental					
Cell number	1	2	3	4	5
Thickness [nm]	75	92	92	98	126
Current Density [mA/cm²]	1.25				

4. Prototype cell housing

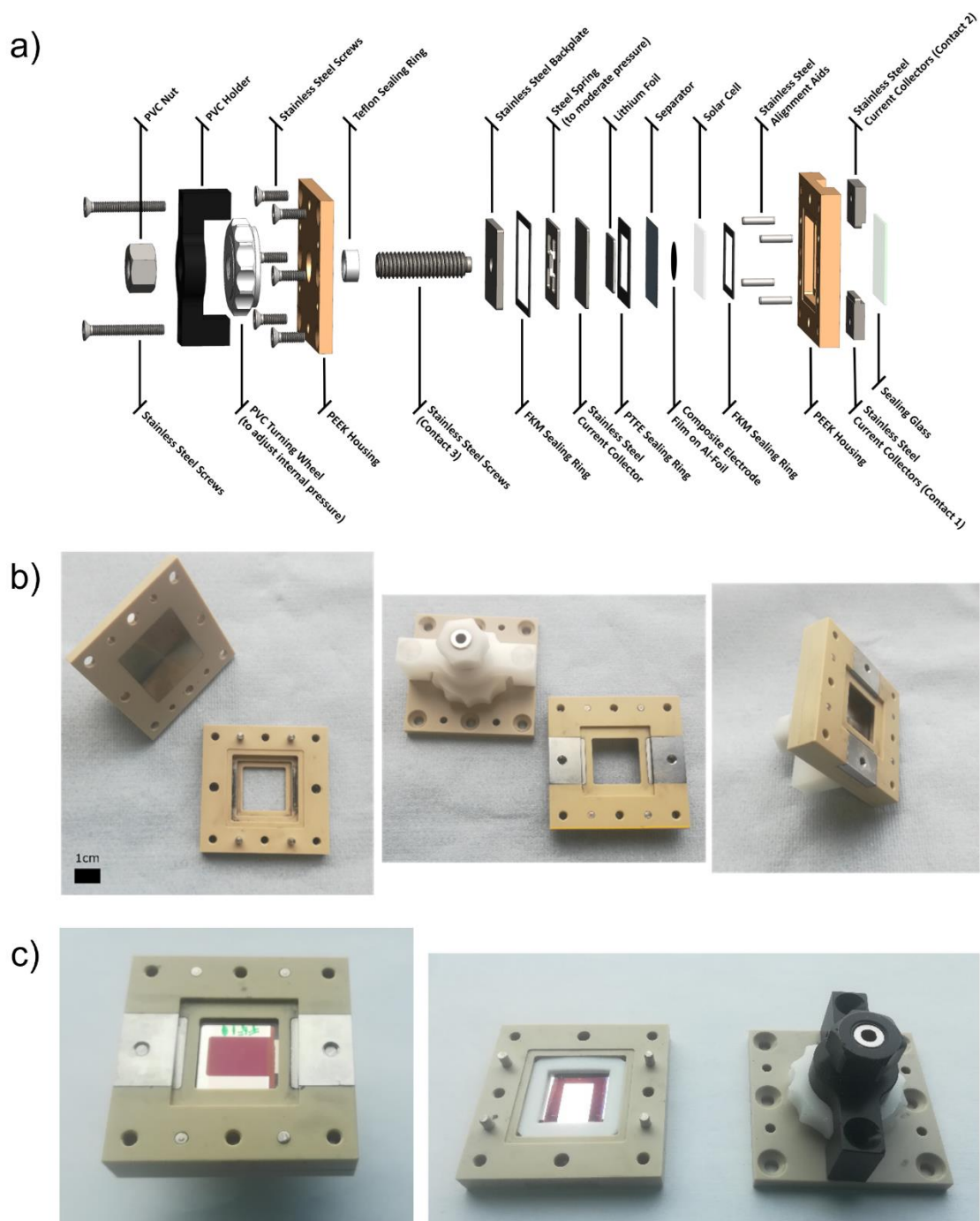


Figure S6: Photo-battery PEEK housing. a) Exploded and labelled CAD view of the photoelectrochemical cell used during the experiments. b) Photographs of top and bottom halves of the cell. c) Photos of the assembled device as used during experiments.

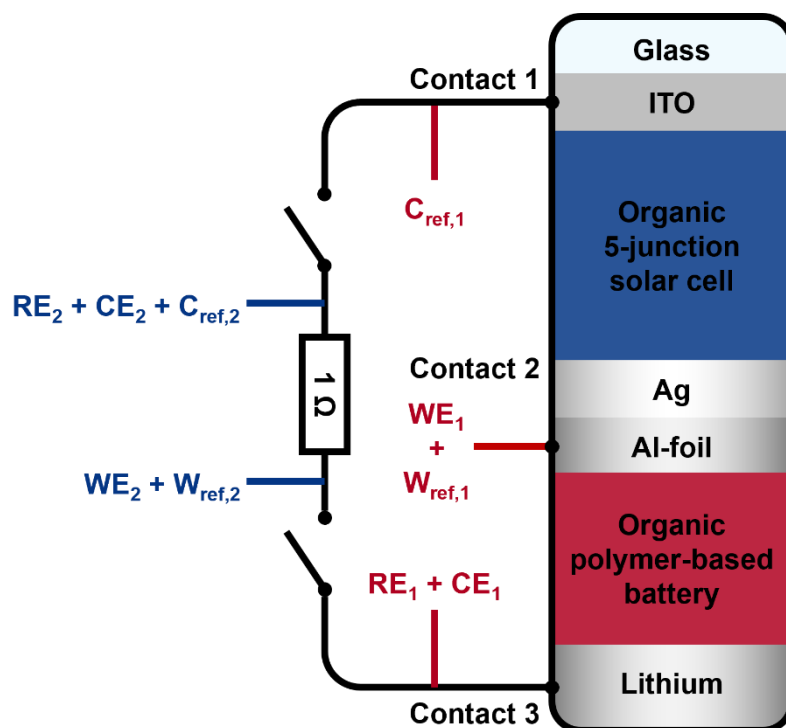


Figure S7: Electrochemical characterization setup scheme. RE: reference electrode, WE: working electrode (defined positive), W_{ref} : reference for the working electrode CE: counter electrode (defined negative), C_{ref} : reference for the counter electrode. Subindices indicate the two different potentiostat channels. The photocharging current is calculated from the voltage drop ($W_{ref,2}-RE_2$) through a resistor of known value (1Ω). The solar cell voltage is defined by the potential difference $W_{ref,1}-C_{ref,1}$ while $W_{ref,1}-RE_1$ measures the battery voltage. The two switches are remotely controlled and close during photocharge as soon as the illumination is started. The dark discharge current is applied between WE_1 and CE_1 .

5. Characterization of the separate parts of the photo-battery

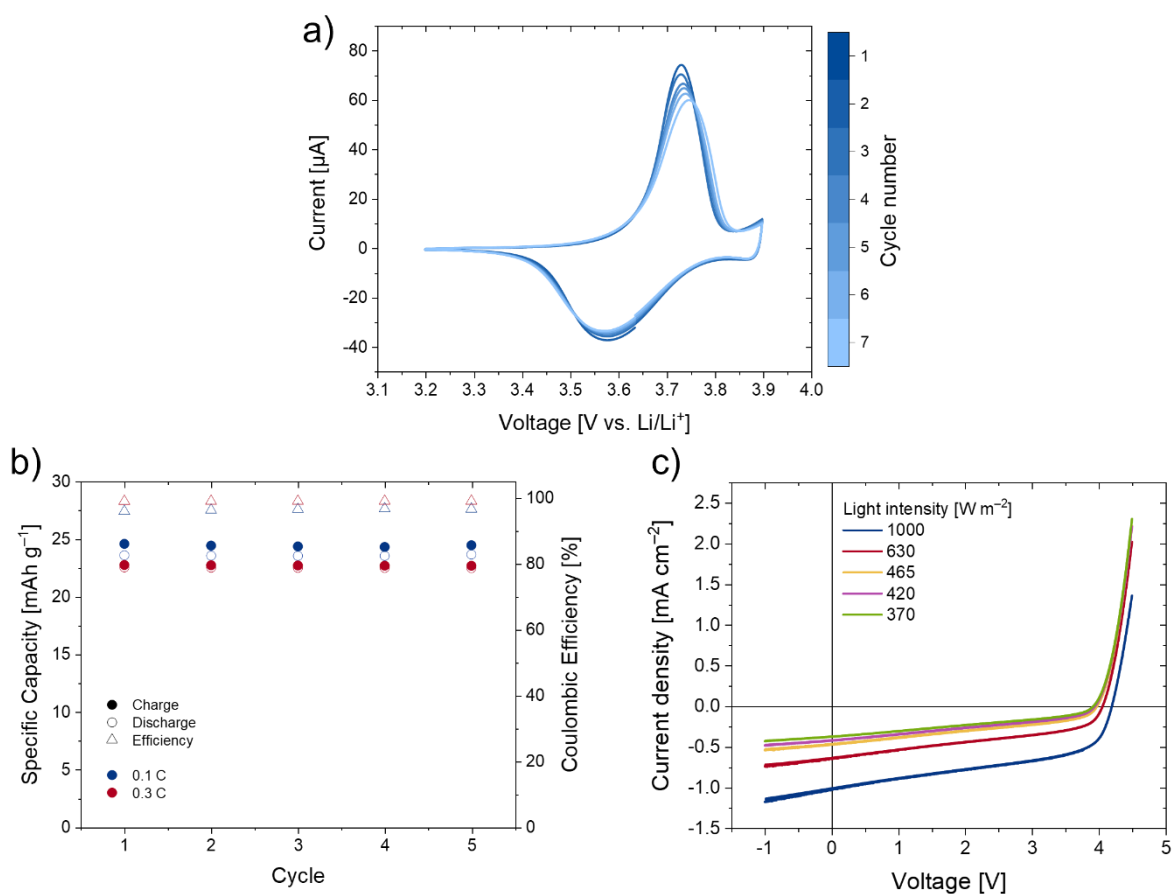


Figure S8: Characterization of the battery and solar cell parts previous to photocharge. a) Cyclic voltammetry traces from the battery after assembly in the photo-battery device holder at 0.1 mV s^{-1} . b) Specific capacity and coulombic efficiency of the battery after assembly obtained from galvanostatic charge-discharge with rates of 0.1 C (2.53 mA g^{-1}) and 0.3 C (12.7 mA g^{-1}). c) JV-curves of the solar cell at different light intensities after assembly in the photo-battery device holder.

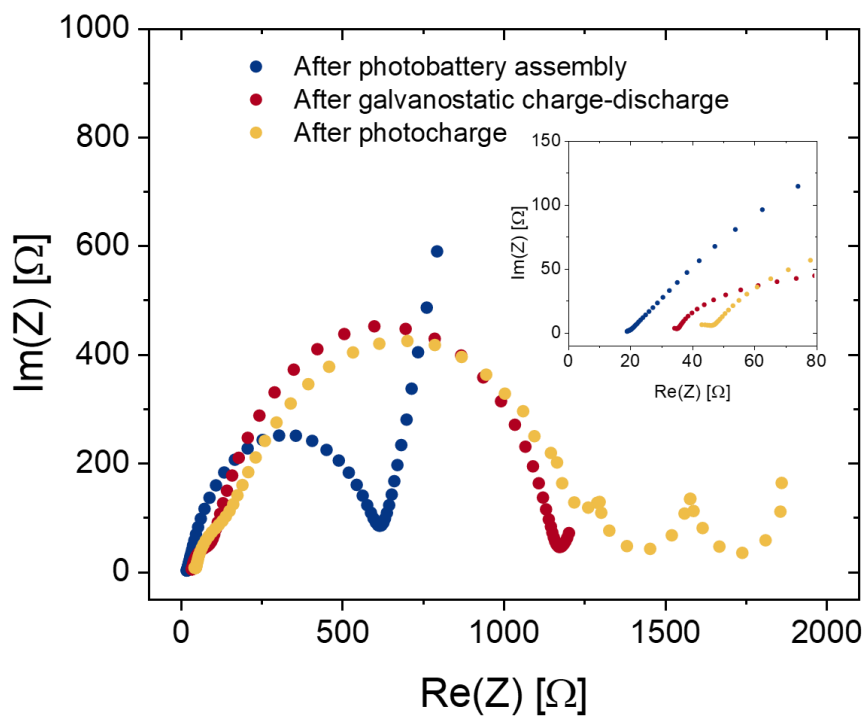


Figure S9: Nyquist plot of electrochemical impedance measurements of the battery part in the photobattery assembly at different points during operation. The inset shows the high frequency part of the spectrum. All the curves were recorded for the discharged state (3.2 V) with a voltage perturbation of 10 mV.

6. Additional photo-battery data

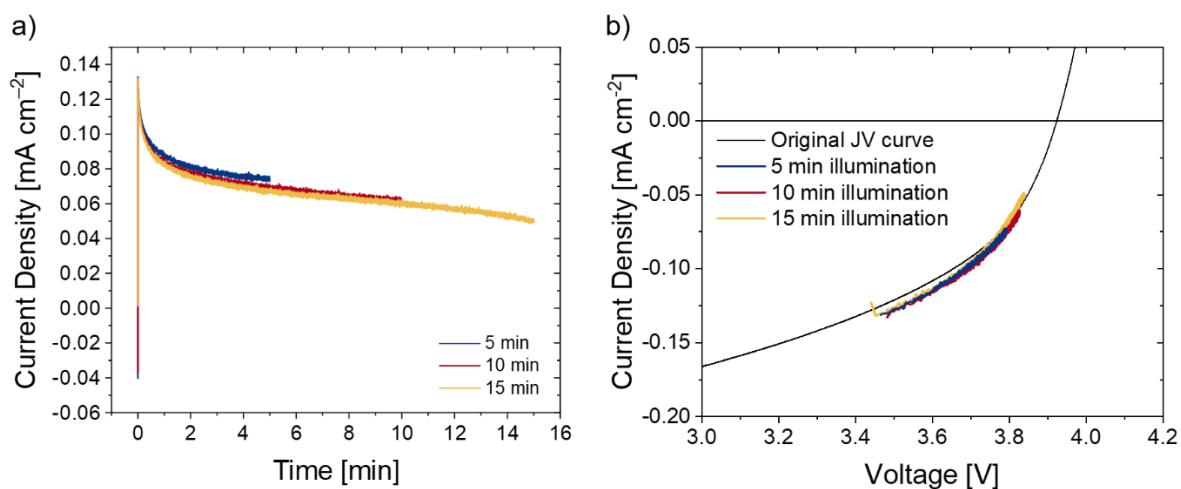


Figure S10: Current normalized to solar cell active area during photocharge experiment. a) Current density over photocharge time. b) Current density vs. solar cell voltage during photocharge, compared with a JV-curve taken before photocharge. By monitoring both the current flowing to the battery (through contacts 1 and 3) and the voltage in the solar cell (using contacts 1 and 2) during the photocharge, reconstructing the solar cell JV curve in this voltage range is possible.

7. Total cycle efficiency calculation.

The total cycle efficiency displayed in Figure 6d is calculated using the following formula.¹

$$\begin{aligned}
 \eta_{\text{cycle}} &= \eta_{\text{conversion}} \times \eta_{\text{storage}} = \frac{E_{\text{solar cell}}^{\text{output}}}{E_{\text{light}}} \times \frac{E_{\text{output}}}{E_{\text{stored}}} \\
 &= \frac{\int_0^{t_c} V_{\text{solar cell}}(t) J_{\text{solar cell}}(t) dt}{\int_0^{t_c} P_1(t) dt} \\
 &\quad \times \frac{\int_{t_c}^{t_d} V_{\text{cap}}(t) J_{\text{GD}}(t) dt}{\int_0^{t_c} V_{\text{cap}}(t) J_{\text{solar cell}}(t) - J_{\text{solar cell}}^2(t) R_{\text{loss}} dt}
 \end{aligned}
 \tag{Equation S3}$$

When ohmic losses between the solar cell and the battery are very low or non-existent, $E_{\text{solar cell}}^{\text{output}} = E_{\text{stored}}$, the cycle efficiency can be simplified to the energy ratio of energy input and output as detailed in the main text. This is true for the data displayed in Figure 6d and as examples, for the first cycle the input is 430 J, and with an output of 6.3 J, their ratio is 0.0146 (1.46 %), while for the last cycle the input is 194 J and with an output of 3.4 J, their ratio is 0.0175 (1.75 %).

8. Ragone plot for photocharge cycling the photo-battery

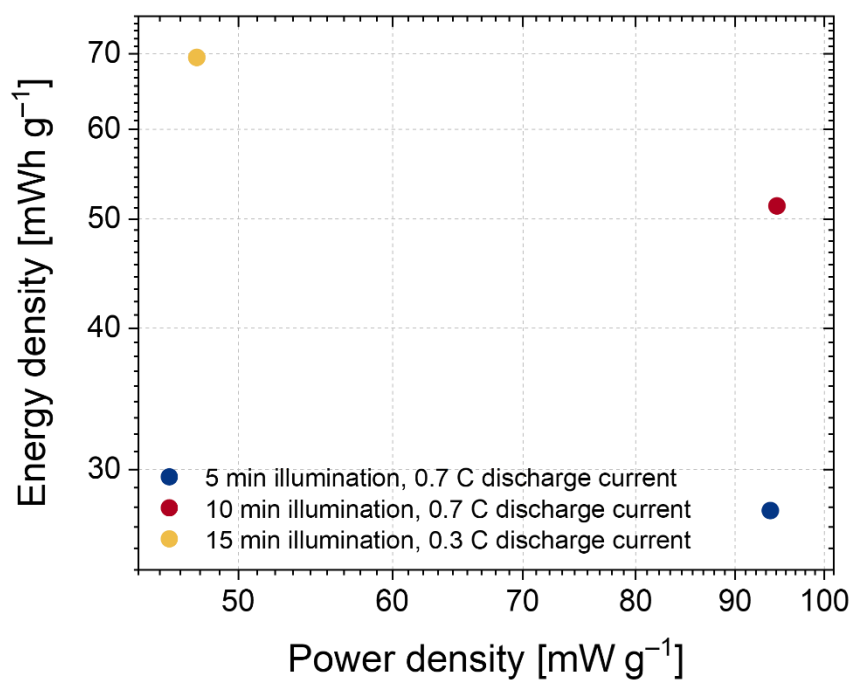


Figure S11: Ragone plot with the results for the photocharge experiment with different illumination times and discharge currents. Each point corresponds to the average value obtained for 10 photocharge-discharge cycles.

9. Redox equations for the charging and discharging processes

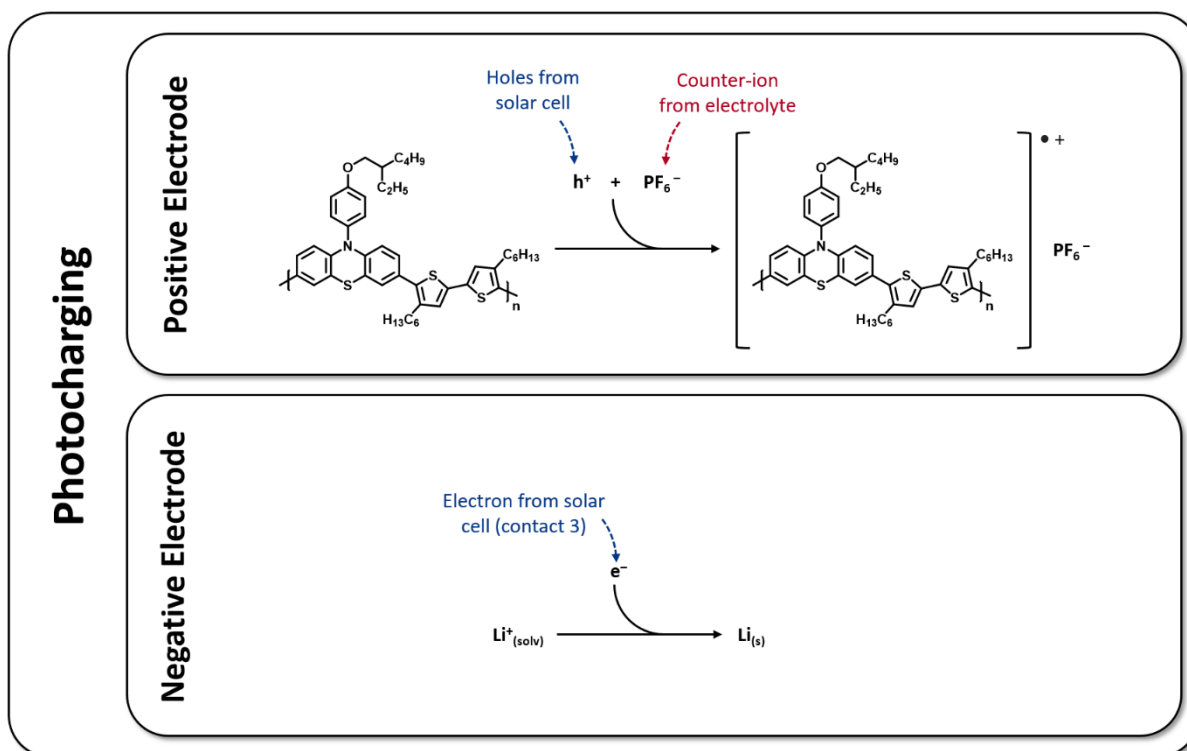


Figure S12: Redox processes during the photocharge of the battery.

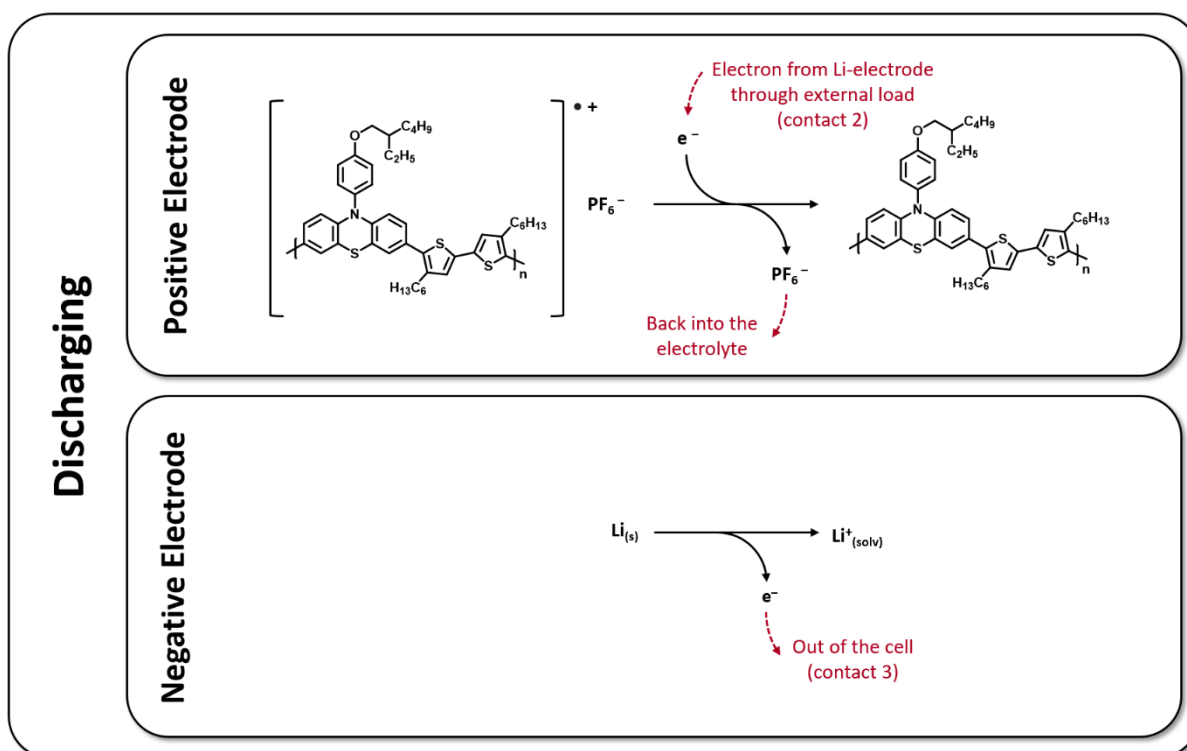


Figure S13: Redox processes during dark discharge of the battery.

10. Comparison of multi-junction solar cells from the literature

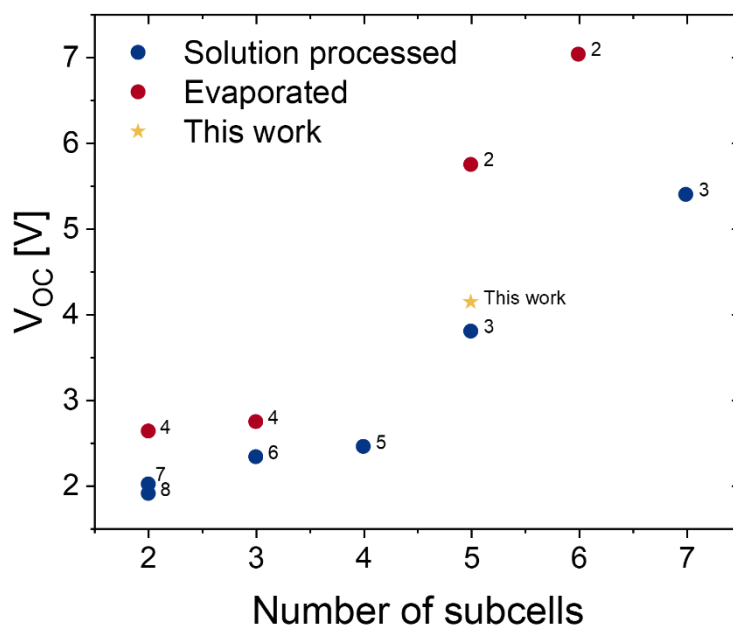


Figure S14: Open-circuit voltage of different organic multi-junction devices from literature as a function of the number of sub-cells used. The respective references indicated by the numbers can be found in Table S6.

Table S6: Parameters of different organic multi-junction cells from literature

Number of sub cells	V _{oc} [V]	Efficiency [%]	Notes	Ref.	Ref. in Manuscript
5	4.14	3.07	This work	/	/
6	7.04	3.0	Evaporated absorber	2	37
5	5.75	3.2	Evaporated absorber	2	37
7	5.4	0.85	Solution processed	3	62
5	3.8	2.1	Solution processed	3	62
3	2.74	9.7	Evaporated absorber	4	64
2	2.63	10.4	Evaporated absorber	4	64
4	2.45	7.6	Solution processed	5	63
3	2.33	5.3	Solution processed	6	65
2	2.01	20.27	Solution processed	7	60
2	1.9	19.64	Solution processed	8	61

11. Comparison of photo-chargeable devices from the literature

Table S7: Literature examples for photo-batteries comparable to the system presented in our manuscript.

Photo-battery system	Average Discharge Voltage [V]	Charging Time	Discharge Capacity	“Overall Efficiency” ^a	Ref.	Ref. in Manuscript
Carbon Nitride / PEDOT:PSS	~ 0.6	Seconds - minutes	~ 2.5 mAh/g	0.002% (1 sun)	9	19
VO ₂ / rGO / Zn	~ 0.6	Minutes - hours	~ 315 mAh/g	0.18% (455 nm LED)	10	23
VO ₂ / rGO / Zn	~ 0.6	Minutes - hours	~ 432 mAh/g	0.51% (455 nm LED)	11	24
PTB7-Th:O-IDTBR Tandem Cell + Li ₃ V ₂ (PO ₄) ₃ / VS ₂ and Na ₃ V ₂ (PO ₄) ₃ / NaTi ₂ (PO ₄) ₃	~ 1.4	Seconds - minutes	~ 50 μAh / cm ²	Max. 1.4% for Li and 0.6% for Na (1 sun)	12	16
DSSC Tandem & Module (N-719 and N-749) + TiO ₂ Nanotubes / LiCoO ₂	~ 2.0	Minutes	~ 39 μA (no specific capacity given)	0.82% (1 sun)	13	20
PBDB-T-2F / PC ₆₀ BM + P(PT-BT) / Li	~ 3.6	Seconds - Minutes	22 mAh/g	1.6% (voltage limit, 1 sun), 1.3% (time limit, 370W/m ²)		This work

^a Calculations for these key values are not generally standardized and differ between publications. Please refer to the respective reference.

12. References

- 1 R. Delgado Andrés, T. Berestok, K. Shchyrba, A. Fischer and U. Würfel, *Sol. RRL*, 2022, **6**, 2200614.
- 2 P. Sullivan, S. Schumann, R. Da Campo, T. Howells, A. Duraud, M. Shipman, R. A. Hatton and T. S. Jones, *Adv. Energy Mater.*, 2013, **3**, 239–244.
- 3 J. Tong, S. Xiong, Y. Zhou, L. Mao, X. Min, Z. Li, F. Jiang, W. Meng, F. Qin, T. Liu, R. Ge, C. Fuentes-Hernandez, B. Kippelen and Y. Zhou, *Mater. Horiz.*, 2016, **3**, 452–459.
- 4 R. Meerheim, C. Körner, B. Oesen and K. Leo, *Appl. Phys. Lett.*, 2016, **108**, 103302.
- 5 D. Di Carlo Rasi, K. H. Hendriks, M. M. Wienk and R. A. J. Janssen, *Adv. Mater.*, 2018, **30**, 1803836.
- 6 S. Esiner, H. van Eersel, M. M. Wienk and R. A. J. Janssen, *Adv. Mater.*, 2013, **25**, 2932–2936.
- 7 Z. Zheng, J. Wang, P. Bi, J. Ren, Y. Wang, Y. Yang, X. Liu, S. Zhang and J. Hou, *Joule*, 2022, **6**, 171–184.
- 8 J. Wang, Z. Zheng, Y. Zu, Y. Wang, X. Liu, S. Zhang, M. Zhang and J. Hou, *Adv. Mater.*, 2021, **33**, 2102787.
- 9 A. Gouder, F. Podjaski, A. Jiménez-Solano, J. Kröger, Y. Wang and B. V. Lotsch, *Energy Environ. Sci.*, 2023, **16**, 1520–1530.
- 10 B. Deka Boruah, A. Mathieson, S. K. Park, X. Zhang, B. Wen, L. Tan, A. Boies and M. De Volder, *Adv. Energy Mater.*, 2021, **11**, 2100115.
- 11 B. Deka Boruah and M. De Volder, *J. Mater. Chem. A*, 2021, **9**, 23199–23205.
- 12 S. F. Hoefler, R. Zettl, D. Knez, G. Haberfehlner, F. Hofer, T. Rath, G. Trimmel, H. M. R. Wilkening and I. Hanzu, *ACS Sustain. Chem. Eng.*, 2020, **8**, 19155–19168.
- 13 W. Guo, X. Xue, S. Wang, C. Lin and Z. L. Wang, *Nano Lett.*, 2012, **12**, 2520–2523.